Advances in Geo-Energy Research

Original article

Investigation of conglomerate softening effect induced by supercritical CO₂-water-rock interaction via micro-scratch test

Liu Yang^{1,2}*, Zhaoyang Liu^{1,2}, Yunhui Lu^{1,2}, Haoru Chen^{1,2}, Yuhang Dong¹, Manchao He^{1,2}

Keywords:

Conglomerate scCO₂-water-rock interaction micro-scratch test micro-mechanical properties micro-structural characteristics

Cited as:

Yang, L., Liu, Z., Lu, Y., Chen, H., Dong, Y., He, M. Investigation of conglomerate softening effect induced by supercritical CO₂-water-rock interaction via micro-scratch test. Advances in Geo-Energy Research, 2025, 18(1): 21-37. https://doi.org/10.46690/ager.2025.10.03

Abstract:

Supercritical CO₂-water-rock interactions significantly impact the mechanical integrity of heterogeneous conglomerate reservoirs, challenging their suitability for CO₂ sequestration and enhanced oil recovery. To evaluate these microscale mechanical and structural changes, this study uses a combination of micro-scratch testing, scanning electron microscopy, and nuclear magnetic resonance. The results reveal that the micro-scratch method enables the acquisition of a continuous mechanical property profile, addressing the limitation of traditional rock mechanics that only allows discrete point measurements. Importantly, the scratch failure modes significantly depend on the lithology of conglomerate reservoirs: Felsic and quartz conglomerates exhibit sharp grooves with interfacial shear failure, whereas debris-rich variants develop wavy, fragmented paths. CO₂-water exposure reduces the deformation resistance and causes fracture toughness to initially increase and then decline, with the most severe reduction observed in quartz conglomerates. The degradation of mechanical properties is mainly through mineral dissolution and increased porosity. The findings of this study offer key insights for optimizing storage and recovery strategies in complex reservoirs.

1. Introduction

Nowadays, fossil fuels contribute over 80% of the global energy supply. However, fossil fuel consumption results in substantial CO₂ emissions, exacerbating global greenhouse effects to a certain extent (Li et al., 2018). In recent years, CO₂ geological sequestration and enhanced oil recovery have emerged as effective alternatives to mitigate the greenhouse effects caused by excessive CO₂ emissions (Richard et al., 2014; Tan et al., 2022). At the high temperatures and pressures encountered in deep reservoirs, the injected CO₂ will be converted from gas to supercritical state. Supercritical carbon dioxide (scCO₂) exhibits unique properties such as high density, excellent solubility, rapid gas diffusivity, and low surface tension (Zhou et al., 2021). The high density of scCO₂ makes it a superior drilling fluid, with its low surface tension

allowing easier penetration into fractures and pores (Esatyana et al., 2021). Consequently, CO₂ has gained considerable attention as a non-aqueous fracturing fluid among researchers in the oil and gas extraction fields (Yang et al., 2016). As unconventional reservoirs, conglomerate reservoirs are characterized by low porosity, low permeability, and poorly sorted gravels with significant strength contrasts among interstitial materials, whereas conventional sandstone reservoirs typically exhibit uniform grain sorting and moderate heterogeneity. This high heterogeneity of conglomerate reservoirs leads to localized stress concentrations and heightened sensitivity to cementation integrity, posing unique challenges for rock mechanical stability when exposed to CO₂, which is often injected into these reservoirs to act as a low-permeability caprock for CO₂ storage and enhance oil recovery (Richard et al., 2014;

Yandy Scientific Press $\ ^{*}Corresponding \ author.$

E-mail address: shidayangliu@126.com (L. Yang); zhaoyangliu1949@163.com (Z. Liu); luyunhui753951@163.com (Y. Lu); chen20230620@163.com (H. Chen); 18801191349@163.com (Y. Dong); hemanchao@263.net (M. He). 2207-9963 © The Author(s) 2025.

Received July 13, 2025; revised August 15, 2025; accepted September 7, 2025; available online September 10, 2025.

¹State Key Laboratory for Tunnel Engineering, China University of Mining and Technology, Beijing 100083, P. R. China

²School of Mechanics and Civil Engineering, China University of Mining and Technology, Beijing 100083, P. R. China

Tan et al., 2022). Furthermore, conglomerate reservoirs may contain pre-existing water, in which injected CO_2 is likely to dissolve, creating a mildly acidic environment that can alter the mechanical properties of reservoirs (Jung et al., 2013; Seyyedi et al., 2020). Given the lack of fundamental insights into these processes, particularly at the nano/microscale, further investigations are essential to explore the potential impacts of CO_2 injection on conglomerate reservoirs.

CO₂-water-rock interaction is complex because of the reversible ionization of carbon acid and the solubility variation of CO₂, which in turn dominates the physicochemical reaction between the media involved (Zhang et al., 2017). Previous studies have shown that the interaction of scCO₂ with rock can significantly weaken the mechanical properties of rock, such as tensile strength, compressive strength, and elastic modulus (Bai et al., 2021). This weakening in strength before and after soaking is positively correlated with soaking pressure and negatively correlated with soaking temperature (Yang et al., 2023). Moreover, scCO₂-water-rock interactions can alter the transport characteristics of rock (Luo et al., 2019). Low viscosity and high diffusivity allow CO₂ to penetrate the micro-pores, inducing the formation of new fractures (Figueiredo et al., 2015; Dong et al., 2020; Nie et al., 2022; Niu et al., 2024). On the one hand, the injected CO₂ generates expansive stress that damages the pore structure of rock, particularly in shale, coal, and sandstones with high clay mineral content (Busch et al., 2008; Zhang et al., 2016, 2018; Nie et al., 2018). On the other hand, CO₂ reacts with formation water to form carbonic acid, causing the dissolution or precipitation of organic matter, clay, feldspar and quartz minerals (Espinoza et al., 2011; Hangx et al., 2013; Zhang et al., 2017; Goodman et al., 2019;). These CO₂-induced reactions depend on factors such as mineral type, reaction temperature, and pressure (Eleni and Lyesse, 2022), and they reshape pore morphology and alter reservoir permeability (Tao et al., 2022). However, the interaction between scCO₂ and rock is a prolonged and complex process, hence further research is necessary to understand the mechanisms of nano-scale interactions between CO₂ and conglomerate.

Many studies have investigated the changes in conglomerates after exposure to CO2 or its solutions, revealing that CO₂-water-rock interactions substantially alter the mechanical strength, pore structure, permeability, and mineralogy. Daphalapurkar et al. (2011) indicated that conglomerates exhibit similar static mechanical properties under scCO₂-water conditions due to their high quartz content (approximately 90%) and stable particle contacts. In short-term experiments, the adsorption of scCO2 on the rock surface was shown to have a minor impact on its mechanical performance, with chemical reactions being negligible. Bello et al. (2024) proved that sandstone subjected to high-temperature heating forms a significant number of dissolution pores after CO2 injection, affecting the storage capacity and physical properties of rock. Additionally, some scholars conducted uniaxial experiments on conglomerates to quantify how CO₂ reduces their strength (Goodman et al., 2019). It was found that the strengths of saturated water, saturated CO₂, and saturated water-CO₂ were reduced by 36%, 13.4%, and 65.7%, respectively. However, these measurements primarily addressed the overall alteration of conglomerates, whereas a comprehensive understanding of CO₂ displacement, sequestration, and storage requires insights into how individual mineral components react to CO₂ exposure. Furthermore, the high heterogeneity of conglomerate reservoirs results in significant spatial variations in mechanical properties at the micro- and nanoscale. To this end, traditional macro-mechanical tests often fail to capture the localized weakening or interfacial degradation caused by scCO₂-waterrock interactions. Nanoscale mechanical behaviors, particularly those of individual mineral components (e.g., quartz, feldspar, and clay), critically influence the overall mechanical response of the rock mass, as dissolution, precipitation and microcracking initiate at mineral boundaries and within weak phases. Therefore, the accurate evaluation of reservoir integrity after CO2 injection requires investigating the nanomechanical properties and specific reactions of each mineral component to CO₂ exposure. With advancements in precision testing instruments such as micro-scratch tests (Richard et al., 2012) and nanoindentation (Shi et al., 2020), it is now possible to obtain the mechanical properties of rock at the nanoscale (Yang et al., 2024a, 2024b). Moreover, micro-scratch tests allow the continuous recording of the mechanical parameters, yielding richer data than the discrete points collected by nanoindentation (Akono et al., 2011).

This study investigated the effects of CO₂ and water treatment on the primary mineral components and used microscratch tests to identify the resulting mechanical changes. The mineral phases were identified using a combination of Quantitative Evaluation of Minerals by scanning electron microscopy (QEMSCAN), scanning electron microscopy (SEM), and energy-dispersive X-ray spectroscopy (EDS), allowing for the establishment of a correlation between the measured mechanical properties and corresponding conglomerate mineral phases. Additionally, nuclear magnetic resonance (NMR) was used to analyze the impact of CO₂ on the pore structure. This research provides a detailed microscopic perspective on CO₂-water-rock interactions, contributing to advancements in CO₂ geological storage and enhanced oil recovery.

2. Experimental methodology

2.1 Sample description and preparation

Conglomerates, as critical components of unconventional reservoirs, are known for their unique compositional structure and high heterogeneity. This study focuses on conglomerates in the Mahu well area of the Junggar Basin, with the geographical location and sample information depicted in Fig. 1. The conglomerate consists of gravel and interstitial material, with a distinct difference between the two. The interstitial material, composed of particle debris with diameters less than 1 mm, further exacerbates the heterogeneity of the conglomerates. Conglomerate reservoirs in the Junggar Basin are generally characterized by poor physical properties, high cementation, and strong water sensitivity, posing severe challenges to oilfield development. Therefore, investigating the impact of scCO₂-water on such complex conglomerates hold significant research value for optimizing oilfield development

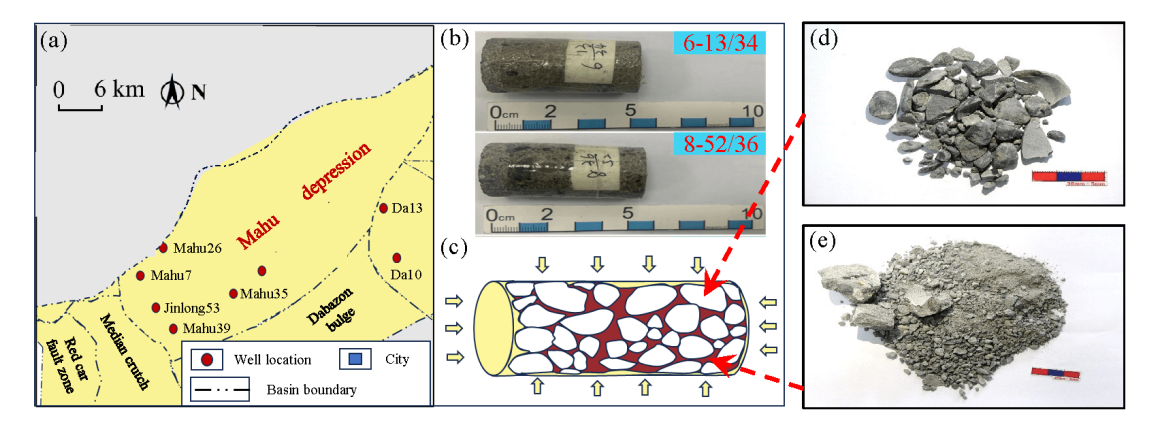


Fig. 1. Overview of the Mahu well area and experimental samples: (a) Overview of the Mahu well area, (b) experimental samples, (c) schematic of CO₂ soaking, (d) gravel and (e) interstitial material.

in unconventional reservoirs.

During the sample preparation, a 50 mm diameter core plug was first dried at 100 °C for 24 hours, then it was cut into 5 mm thick discs. A flat surface is necessary for microscratch tests to guarantee accuracy and consistency (Donnelly et al., 2006). Therefore, the conglomerate disk underwent a precise polishing procedure using abrasive papers from P1,200 to P4,000. To reach a finer surface, the remaining samples were further polished using 1 µm polycrystalline diamond suspension, 0.25 µm polycrystalline diamond suspension, and 0.05 µm alumina suspension. After the polishing process, the surfaces of the samples were cleaned with ethanol. An optical profilometer was used to check the roughness of the polished surfaces. According to established methodologies for controlling surface roughness in nanoindentation and micro-scratch tests (Vandamme et al., 2010; Sakulich and Li, 2011), the following criterion was strictly followed to ensure measurement accuracy: Within a scanning area with a side length equal to 200 times the minimum indentation depth (≈ 100 nm) employed in this study, the root mean square (RMS) roughness (Ra) was controlled to be less than one-fifth of the indentation depth. Furthermore, in line with the recommendation by Akono et al. (2012) for the microscratch testing of brittle materials, the sample surface Ra was further constrained within an order of magnitude smaller than the minimum scratch depth, ultimately maintained below 50 nm. This dual criterion ensures that surface roughness-induced interference is negligible relative to the micro-mechanical signals of interest. Furthermore, this experiment employs SEM to scan the sample surface to reveal the morphology, composition and structural characteristics. Concurrently, NMR technology was utilized to analyze the T_2 transverse relaxation times and T_1 - T_2 spectroscopic features in the pores.

In the first round of micro-scratch tests, SEM-EDS, and QEMSCAN analyses were performed on the polished conglomerate sample to obtain its baseline mechanical and mineralogical properties. Then, conglomerate samples were treated with scCO₂-water for 8, 16, and 24 d. After 10 and 20 d of fluid treatment, second-round and third-round micro-scratch tests were conducted on the samples. After 24 d of treatment, a fourth round of micro-scratch tests was conducted, fol-

lowed by QEMSCAN-SEM-NMR analysis. QEMSCAN analysis provides the mineralogy information of the conglomerate samples; micro-scratch tests can characterize the mechanical properties of conglomerate before and after treatment; SEM assists to locate the scratch and offers the morphology of the residual impression; whereas NMR provides information regarding the pore structure. By combining the QEMSCAN-SEM-NMR results with micro-scratch tests, the mineralogy related mechanical change can be directly observed.

2.2 Micro-scratch tests

Micro-scratch tests were performed using a Keysight G200 system equipped with a Berkovich indenter (Fig. 2). To ensure data reliability, three independent parallel scratch tests were conducted on each sample, with adjacent scratches spaced 60 µm apart to eliminate stress interference (Randall et al., 2009). The micro-scratch mechanical parameters (e.g., scratch depth, fracture toughness) of conglomerate samples were quantitatively evaluated by the coefficient of variation, demonstrating experimental reproducibility. Post-immersion morphological characterization was performed using a HELIOS 5CS Environmental SEM microscope, while SEM and QEMSCAN observation were repeated across all scCO₂-water-treated samples to confirm mineralogical homogeneity. This multi-tiered validation framework ensures both mechanical and compositional consistency throughout the experimental protocol.

Scratching is a fracture-dominated process that enables the evaluation of fracture performance at a highly refined scale (Liu et al., 2023). Scratch fracture toughness refers to the resistance of a material to fracture when subjected to scratching, while fracture toughness reflects its ability to resist crack propagation. The latter is calculated from a micro-scratch test using the following formula (Akono and Kabir, 2016):

$$K_{IC} = \frac{F_T}{\sqrt{2p(d)A(d)}}\tag{1}$$

where K_{IC} represents the fracture toughness, MPa·m^{1/2}; F_T represents the cutting force, mN; d represents the scratch depth μ m; p(d) represents the scratch perimeter at depth d, μ m; and A(d) is the projected contact area at depth d, μ m².

Scratch hardness reflects the resistance of a material to

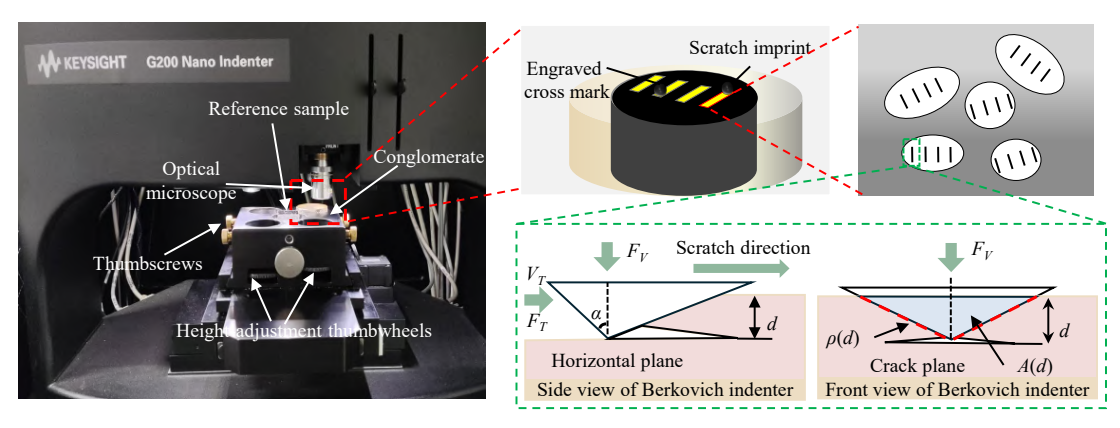


Fig. 2. Schematic of the micro-scratch testing principle.

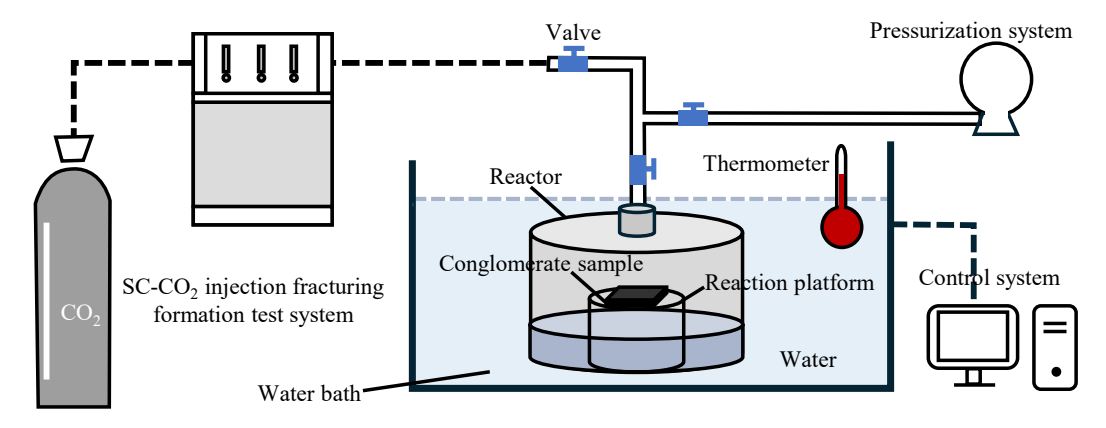


Fig. 3. Flowchart of the CO₂ immersion test.

deformation (Liu et al., 2023):

$$H = \frac{F_V}{A(d)} \tag{2}$$

where H denotes the scratch hardness, MPa; and F_V is the normal force, mN.

For a Berkovich indenter, that features a three-sided pyramidal tip with a well-defined facet angle, its scratch perimeter p(d) is derived based on the projection geometry during the scratching process. Specifically, during scratching, p(d)represents the perimeter of the projected contact area at depth d and is calculated as the sum of the edge lengths L_{AE} and L_{AC} along the scratching direction (see Fig. 2).

The length L_{AE} and L_{AC} correspond to the projection of the indenter edge at depth d, given by:

$$L_{AE} = d\sqrt{1 + \frac{4\tan^2\beta \cdot \cos^2\theta}{3\cos^2\alpha}}$$
 (3)

$$L_{AE} = d\sqrt{1 + \frac{4\tan^2\beta \cdot \cos^2\theta}{3\cos^2\alpha}}$$

$$L_{AC} = d\sqrt{1 + \frac{4\tan^2\beta \cdot \sin^2(30^\circ + \theta)}{3\cos^2\alpha}}$$
(3)

Thus, the scratch perimeter p(d) is

$$p(d) = L_{AC} + L_{AE} = d \cdot \left(\sqrt{1 + \frac{4 \tan^2 \beta \cdot \cos^2 \theta}{3 \cos^2 \alpha}} + \sqrt{1 + \frac{4 \tan^2 \beta \cdot \sin^2 (30^\circ + \theta)}{3 \cos^2 \alpha}} \right)$$
 (5)

where θ represents the apex angle of the Berkovich indenter (130.6°), and β and α are constants related to the indenter shape for a Berkovich indenter ($\beta = 70.05^{\circ}$ and $\alpha = 65.3^{\circ}$).

This expression simplifies to the form Eq. (7) (Akono and Ulm, 2017), consistent with prior literature. Here, A(d)is proportional to d^2 and p(d)A(d) is proportional to d^3 , as validated through geometric scaling. The formulas for A(d)and its derivation are similarly grounded in the indenter's projection:

$$A(d) = \tan \theta \left[\tan \alpha + \tan \beta \right] d^2$$

$$p(d) = d\sqrt{1 + \tan \theta \left(\tan \alpha + \tan \beta \right)}$$
(6)
$$(7)$$

$$p(d) = d\sqrt{1 + \tan\theta \left(\tan\alpha + \tan\beta\right)} \tag{7}$$

2.3 CO₂ and water treatment process

The schematic of the CO₂ and water treatment process is shown in Fig. 3. The experimental setup was designed to replicate subsurface conditions relevant to CO₂ geological storage, with specific parameters detailed in Table 1. Dry CO₂ was injected into the treatment vessel at a pressure of 1,500 psi (10.34 MPa). A thermostatic water bath maintained the system temperature at 70 °C, exceeding the critical temperature of CO₂ (31.04 °C). The system pressure was continuously monitored to ensure it was above the critical pressure of CO₂ (7.3) MPa), guaranteeing that CO₂ remained in a supercritical state throughout the experiment (Fatah et al., 2021). The selected pressure and temperature conditions corresponded to typical

Table 1. Basic experimental parameters.

Parameter	Value	Rationale
Pressure	10.34 MPa (1,500 psi)	Exceeds scCO ₂ critical pressure (7.38 MPa)
Temperature	70°C	Exceeds scCO ₂ critical temperature (31.04 °C)
Brine composition	2% NaCl + 1% KCl	Simulates formation water; inhibits clay swelling
CO ₂ phase	Supercritical (scCO ₂)	Mimics CO ₂ behavior in deep reservoirs
Soaking duration	0, 8, 16, 24 d	Captures short/medium term interaction dynamics

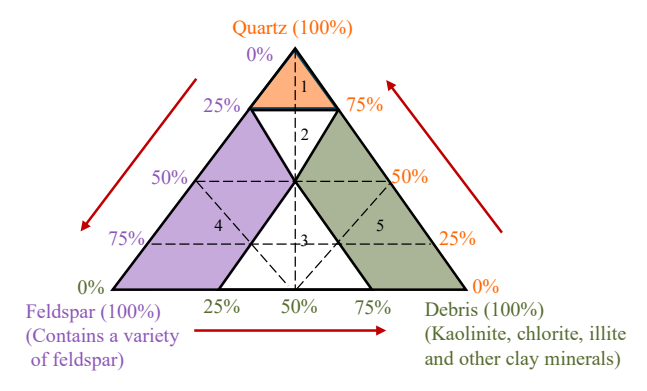


Fig. 4. Ternary map of conglomerate minerals: 1–quartz conglomerate , 2–subfeldspathic debris conglomerate, 3–feldspar debris conglomerate, 4–feldspar conglomerate and 5–debris conglomerate.

reservoir depths of 800-1,500 m, aligning with geological storage scenarios. Additionally, the brine solution (2% NaCl and 1% KCl) was employed to inhibit clay swelling and simulate formation water chemistry (Zhang et al., 2016). To investigate the time-dependent effects of $\rm CO_2$ -water-conglomerate interactions, the soaking durations were set at 0, 8, 16, and 24 d.

3. Experimental results

3.1 Mesoscopic lithofacies categories

The ternary map for conglomerate classification is shown in Fig. 4. Based on mineral content and composition, conglomerates can be classified into different types. In this study, conglomerates were categorized into five lithologies according to the proportions of quartz, feldspar and debris (kaolinite, chlorite, illite, and other clay minerals): Feldspar debris conglomerate, subfeldspathic debris conglomerate, feldspar conglomerate, quartz conglomerate, and debris conglomerate. The QEMSCAN energy-dispersive spectrometer determines elemental information at each point, and the mineral composition and distribution in the target area are derived from the intensity and concentration of these elements. The original QEMSCAN scanning results for the conglomerate samples are shown in Fig. 6.

The ternary diagrams and QEMSCAN results reveal the compositional constituents of conglomerates. Quartz conglomerate (Fig. 4, area labeled 1) is predominantly composed of quartz, with a content ranging from 75% to 100%, and contains approximately 76% quartz, 8% albite and 16% chlorite (Fig. 5(d)). Subfeldspathic debris conglomerate (Fig. 4, area labeled 2) has a quartz content between 50% to 75%, and contains approximately 56% quartz, 24% albite, and 15% chlorite (Fig. 5(a)). Feldspar debris conglomerate (Fig. 4, area labeled 3) contains quartz (0% to 50%), debris (25% to 75%), and feldspar (25% to 75%), and is composed of approximately 39% quartz, 33% albite, and 22% chlorite (Fig. 5(c)). Feldspar conglomerate (Fig. 4, area labeled 4) has quartz (0% to 75%), debris (0% to 25%), and feldspar (25% to 100%), and contains approximately 18% quartz, 61% albite, and 21% chlorite (Fig. 5(b)). Debris conglomerate (Fig. 4, area labeled 5) contains quartz (0% to 75%), debris (75% to 100%), and feldspar (0% to 25%), and is composed of approximately 21% quartz, 36% kaolinite, and 41% chlorite (Fig. 5(e)).

3.2 Failure modes of different lithologies

The current study considers two distinct failure modes: Detile and brittle (Nesbitt and Young, 1984; Crundwell, 2017). The most prominent fragmentation pattern in the brittle regime is caused by the initiation and propagation of tensile macrocracks. Figs. 6(a) and 6(c) show typical cutting force variations corresponding to the propagation of tensile macro-cracks. This phenomenon can be divided into two stages. In the first stage (OA), the nano-indenter compresses the rock as it moves along the sample surface, resulting in an increase in cutting force. Upon reaching the peak at point A, the failure mode shifts to the second stage (AB). In this stage, as the scratch indenter advances, the cutting force decreases, which corresponds to the propagation of tensile cracks. The expansion of these tensile cracks reduces the load-bearing capacity of the rock, causing local failure in front of the scratch indenter. As the scratch indenter continues to move, the cutting force amplitude sharply decreases, accompanied by rock fragment breakage (Randall et al., 2009).

The typical cutting force variations are associated with ductile failure (Figs. 6(b) and 6(d)). This phenomenon is also divided into two stages. In the first stage (OA), the scratch indenter moves along the sample surface, leading to an increase in cutting force. Upon reaching the peak at point A, the failure mode transitions to the second stage (AB). With the scratch displacement increasing, the cutting force in the AB segment exhibits minor fluctuations. This lack of rapid strain energy release in the AB segment is referred to as "plastic flow" (Richard et al., 2012).

During the scratch process, the fragments are discharged along both sides in front of the cutter tip. Scratching the rock surface causes a groove to form that penetrates to a certain depth in the rock, and the cracks are referred to as "thickness cracks". The mode of failure between the groove and the surrounding minerals is termed interfacial failure mode (Bull, 1991). The delamination failure mode delineates the morphological characteristics of rock deformation under

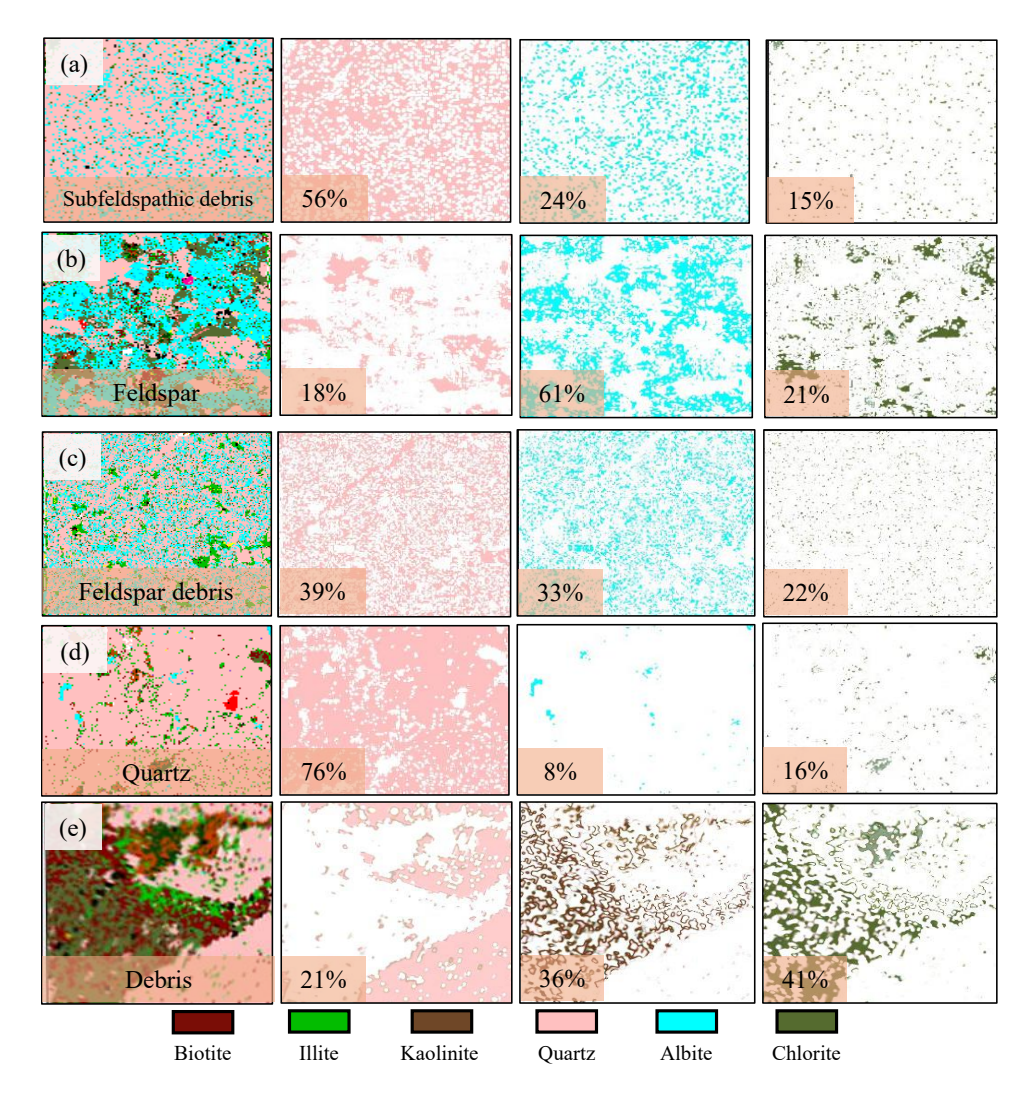


Fig. 5. Lithologic classification map: (a) Subfeldspathic debris conglomerate, (b) feldspar conglomerate, (c) feldspar debris conglomerate, (d) quartz conglomerate and (e) debris conglomerate.

micro-scratch actions, thereby reflecting the intrinsic properties of the rock. The scratch damage morphologies of different conglomerates are illustrated in Fig. 7. During the scratching process, shear failure occurs, resulting in subsequent crack propagation to the scratch interface edge. The scratch interface presents a smooth and linear appearance, while the damaged groove exhibits a sharp and fractured morphology. The scratch width ranges from 2 to 5 μ m, with a relatively narrow width. Among the conglomerates, the feldspar debris conglomerate has the largest scratch width (around 5 μ m) while the feldspar, subfeldspathic and quartz conglomerates show smaller scratch widths (approximately 2 μ m).

The morphology of scratch damage in debris conglomerate differs significantly from other conglomerates, as shown in Fig. 7(e). Debris conglomerate contains abundant clay pores that are disrupted during the scratch process. The groove in the clay exhibits a fragmented failure pattern, with a scratch width ranging from 5 to 10 μ m, indicating a larger scratch width. The red bands mark the interfacial failure zones between the clay groove and the surrounding minerals (Fig. 7). The edges of the scratch interface display a wavy pattern, without a distinct

interfacial failure zone, which is due to stress concentration of the scratch between the groove and adjacent minerals.

3.3 Mechanical alterations after scCO₂-water treatments

3.3.1 Scratch deformation

The depth-displacement curve illustrates the relationship between indenter penetration and sample deformation (Fig. 8). The scratch depth represents the penetration depth of the indenter tip into the sample surface and corresponds to the resultant sample deformation. At the end of the indenter cutting, the sample exhibits its maximum deformation. The initial maximum deformation of feldspar debris conglomerate, subfeldspathic debris conglomerate, quartz conglomerate and debris conglomerate are 1,228.47, 873.11, 1,183.87, 489.94, and 10,306.7 nm, respectively. The less the deformation is, the harder the sample. Among them, the debris conglomerate has the largest amount of deformation, with a "parabolic" distribution of curve, while the quartz conglomerate has the smallest scratch deformation, corresponding to the highest har-

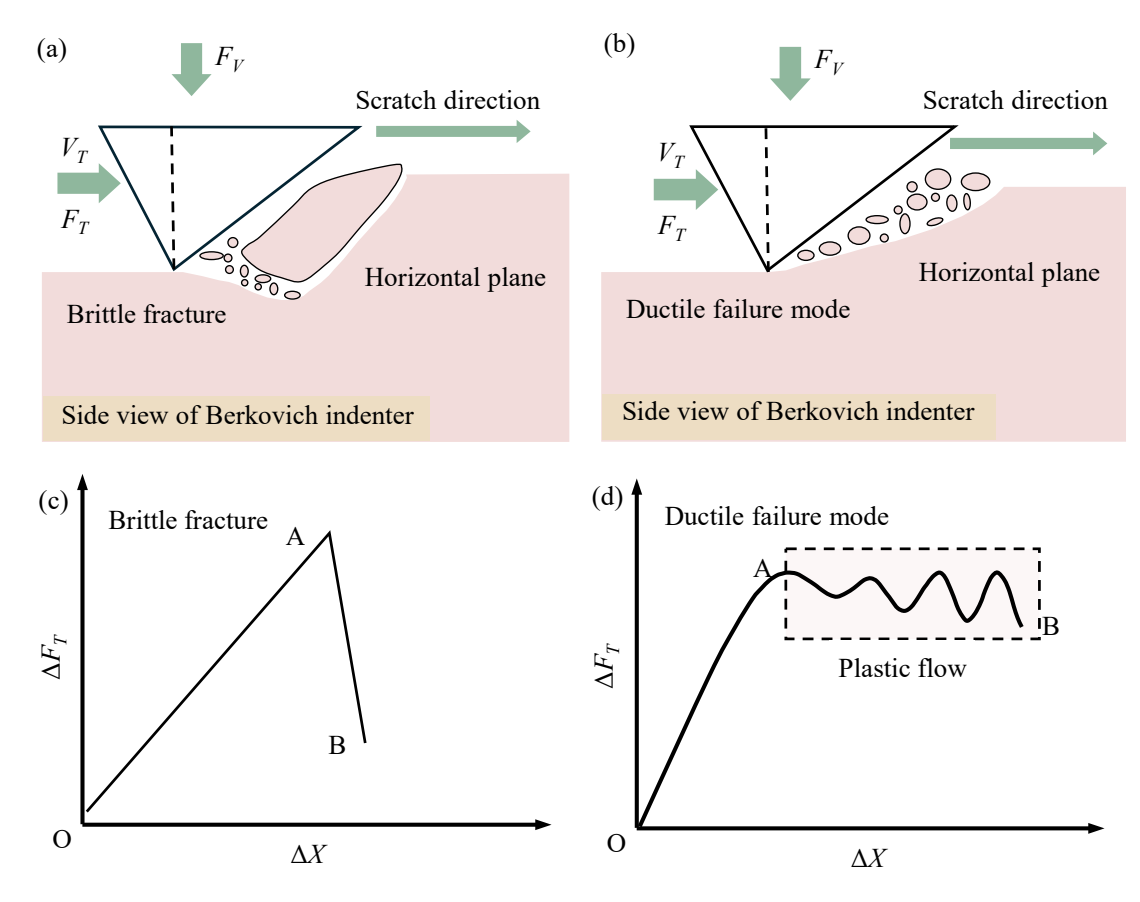


Fig. 6. Morphological characteristics of scratch depth-displacement curves: (a) Brittle damage pattern, (b) plastic damage pattern, (c) brittle damage curve and (d) plastic damage curve.

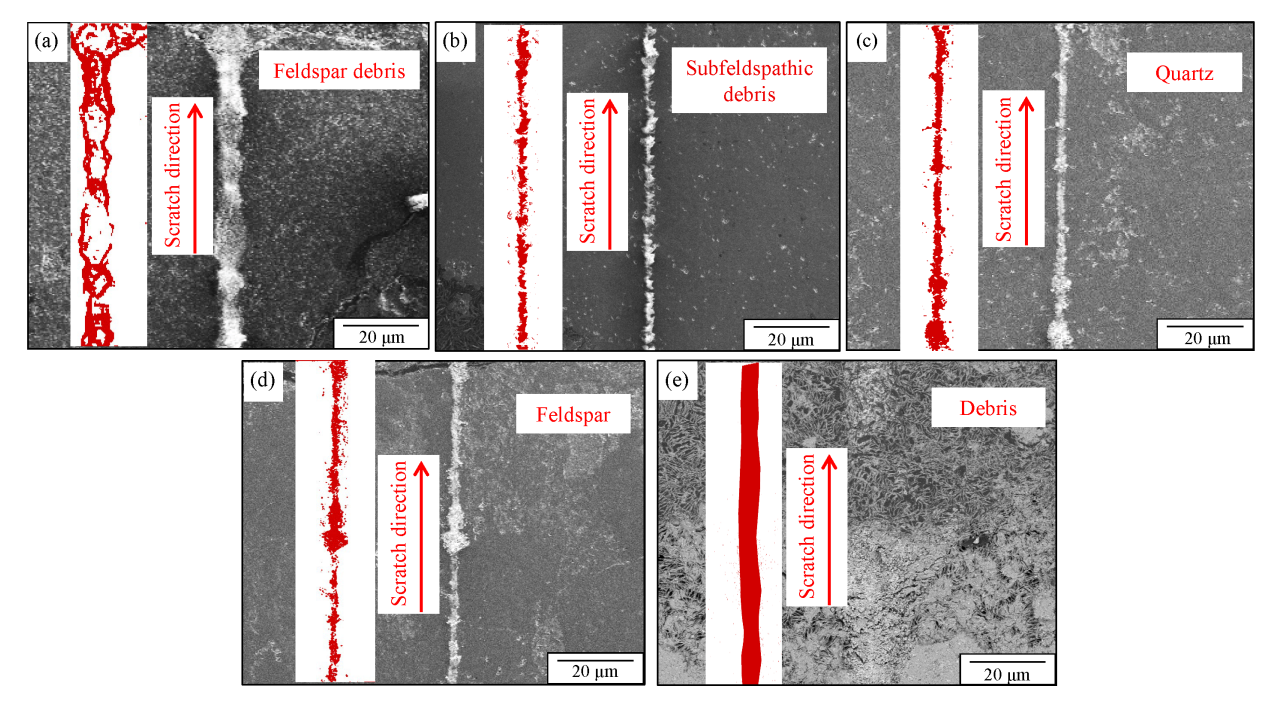


Fig. 7. Typical brittle scratch patterns: (a) Feldspar debris conglomerate, (b) subfeldspathic debris conglomerate, (c) quartz conglomerate, (d) feldspar conglomerate and (e) debris conglomerate.

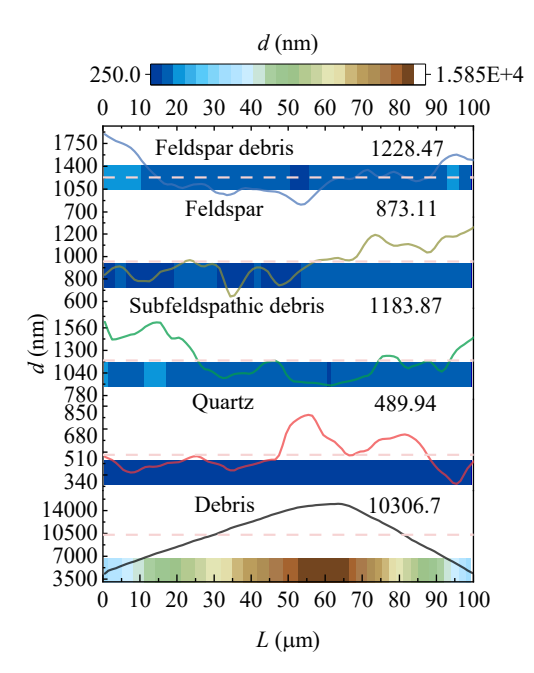


Fig. 8. Scratch depth-displacement curves of conglomerates with different lithologies.

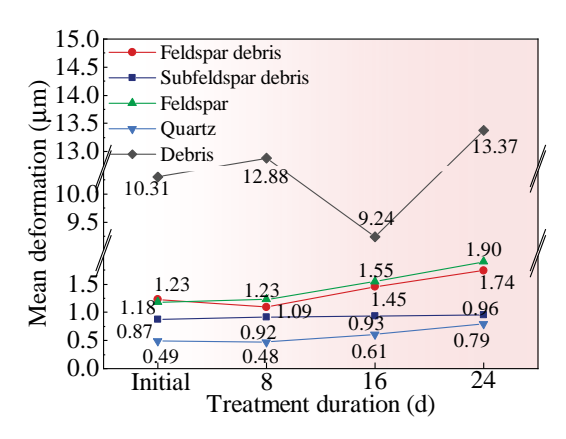


Fig. 9. Evolution of mean deformation under different immersion times.

dness. The curves of the remaining conglomerates are uneven. After the soaking treatment experiment, different types of clastic conglomerates were shown to exhibit unique trends in maximum deformation. As shown in Fig. 9, the feldspar debris conglomerate demonstrates a significant decrease in maximum deformation in the early stages of soaking treatment. However, as the soaking time extends, the maximum deformation gradually increases. In contrast, the subfeldspathic debris conglomerate shows a slight continuous increase in maximum deformation throughout the soaking treatment process. For feldspar conglomerate, the maximum deformation only slightly increases to 1,227.28 nm in the early stages, while in the subsequent soaking treatment, its maximum deformation shows a significant increase. Quartz conglomerate, due to its high hardness, is relatively less affected by soaking treatment and shows a limited increase in maximum deformation. The maximum deformation of debris conglomerate is the most complex and variable: In the early stages of soaking treatment,

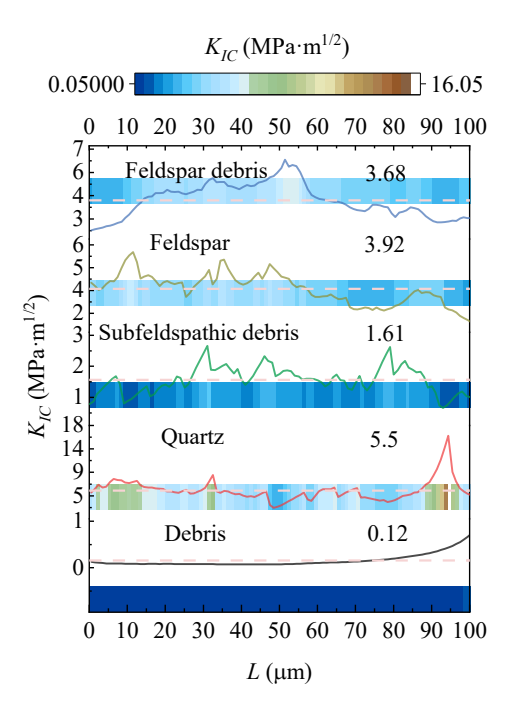


Fig. 10. Scratch fracture toughness-displacement curve.

its maximum deformation increases from 10,306.7 to 12,880.61 nm; however, after 16 d of soaking treatment, it significantly decreases to 9,241.46 nm; after 24 d of soaking treatment, it notably increases to 13,372.68 nm, showing a nonlinear and fluctuating pattern of change.

The maximum deformations of the five samples demonstrate an increasing trend after scCO₂-water treatment, indicating a deterioration of resistance to load. After 24 d of scCO₂-water treatment, the maximum deformation of feldspar debris conglomerate, subfeldspathic debris conglomerate, feldspar conglomerate, quartz conglomerate, and debris conglomerate increases by 41.49%, 9.53%, 60.62%, 61.65%, and 29.74%, respectively. The maximum deformation of feldspar conglomerate and quartz conglomerate increases the most significantly during fluid treatment, while subfeldspathic debris conglomerate exhibits the smallest change. This indicates that the fluid treatment has the most obvious effect on reducing the deformation resistance of feldspar and quartz conglomerate.

3.3.2 Fracture toughness

The fracture toughness curves obtained from micro-scratch tests (Fig. 10) show that the initial values of feldspar debris conglomerate, feldspar conglomerate, subfeldspathic debris conglomerate, quartz conglomerate, and debris conglomerate are 3.68, 3.92, 1.61, 5.5, and 0.12 MPa·m¹/², respectively. Among them, the fracture toughness of the debris conglomerate shows a "concave" curve, while the curves of other conglomerates present a serrated distribution. The fracture toughness of quartz conglomerate is the largest, and that of debris conglomerate is the smallest. The color mapping of fracture toughness reveals that the number of colors mapped in the debris conglomerate is small and the color distribution is uniform, which indicates that the fracture toughness of conglomerate is evenly distributed. The number of colors mapped by the quartz conglomerate is large and the color distribution

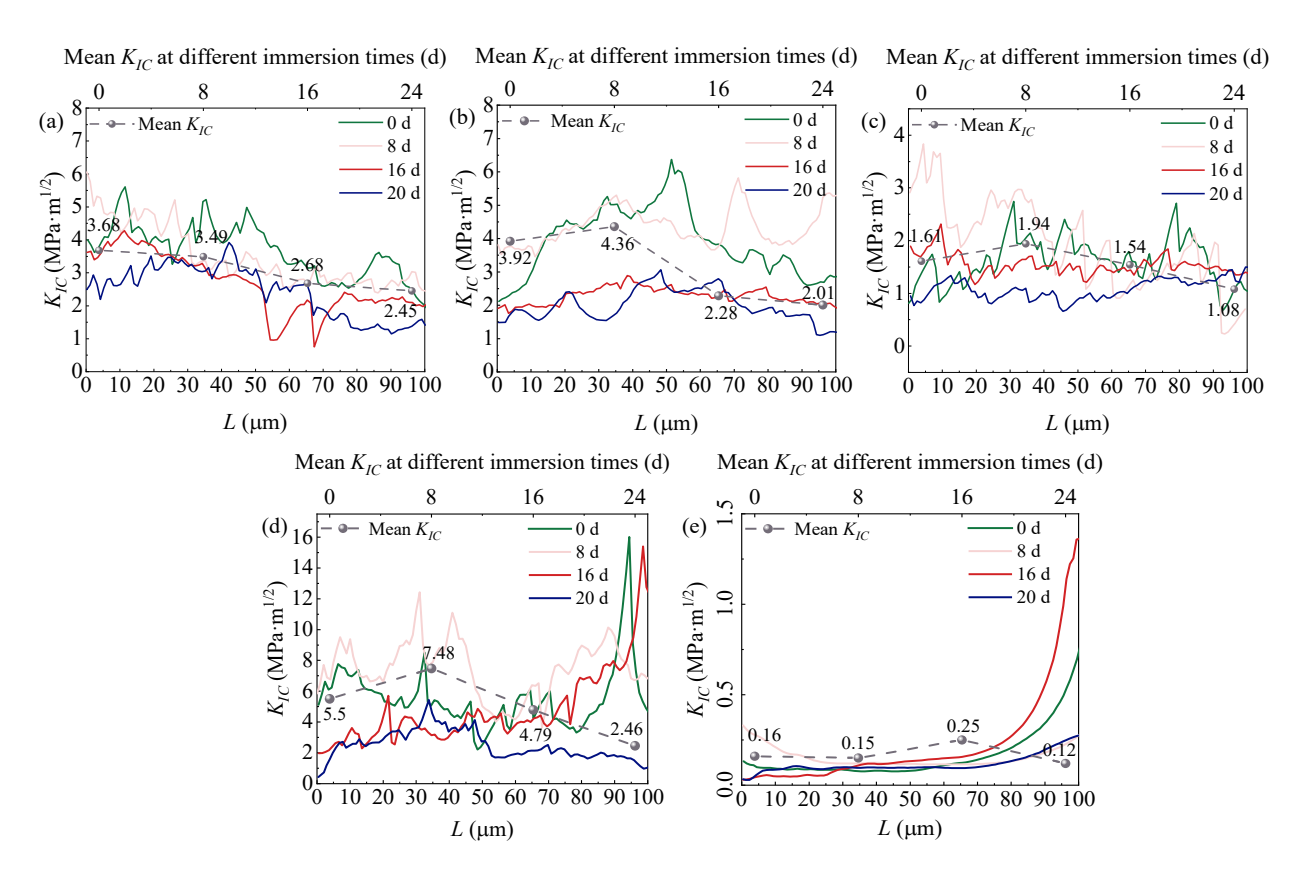


Fig. 11. Evolution of fracture toughness with immersion time: (a) Feldspar debris conglomerate, (b) subfeldspathic debris conglomerate, (c) feldspar conglomerate, (d) quartz conglomerate and (e) debris conglomerate.

fluctuates greatly. This indicates that the fracture toughness distribution is not uniform in the quartz conglomerate.

The changes in the fracture toughness of conglomerate samples are shown in Fig. 11. With increasing soaking time, the fracture toughness curve of feldspar conglomerate shows a linear decline. The fracture toughness curves of subfeldspathic debris conglomerate, feldspar conglomerate and quartz conglomerate increase first and then decrease. The debris conglomerate shows a change trend of first decreasing, then rising and decreasing again. Finally, after 24 d of scCO₂water treatment, the fracture toughness of the five samples all witness a decrease to varying degrees, especially in quartz conglomerate. The average fracture toughness of feldspar debris conglomerate, subfeldspathic debris conglomerate, feldspar conglomerate, quartz conglomerate, and debris conglomerate decrease by 33.42%, 48.72%, 32.50%, 55.27%, and 25.00%, respectively. In general, the decreasing rate of micromechanical parameters is related to the time effect: The longer the immersion time, the greater the decrease in micromechanical parameters.

In order to facilitate the direct comparison of mechanical degradation across the five conglomerate types over time, Table 3 integrates the key parameters: The maximum scratch deformation and fracture toughness for each conglomerate at 0 and 24 d. To highlight the evolutionary trends, the percentage changes relative to the initial state (0 d) are also provided.

The results of fracture toughness density distribution are illustrated in Fig. 12. The peak density values of fracture

toughness exhibit a leftward shift, and the curves before and after immersion belong to normal distribution. For the feldspar debris conglomerate, subfeldspathic debris conglomerate and debris conglomerate, the peak initially increases and then decreases with prolonged exposure to scCO₂-water. For the feldspar conglomerate, the peak first decreases and then increases with the immersion time increasing. Despite the differences observed in peak variations among these four conglomerate samples, there is a consistent overall trend of increasing final peak values, which aligns with previously reported scCO₂-induced mineral dissolution and reprecipitation processes that homogenize mechanical properties over time (Eleni and Lyesse, 2022; Yang et al., 2023). After 24 d of treatment, the peak density values of the four samples exhibit various degrees of increase, and the subfeldspathic debris conglomerate shows the most significant increase in fracture toughness. The peak density values for feldspar debris conglomerate, subfeldspathic debris conglomerate, feldspar conglomerate, and debris conglomerate show an increase of 23.26%, 61.76%, 44.71% and 24.33%, respectively.

Furthermore, it is noteworthy that the changes in peak density for quartz conglomerate are relatively minor, suggesting that scCO₂-water has a limited impact on the mechanical uniformity of quartz. The variations in nano-mechanical properties observed in conglomerate are related to the different mineral compositions, which demonstrates a range of reactions with CO₂-water. A detailed discussion on the dissolution and precipitation of the involved minerals will be provided in the

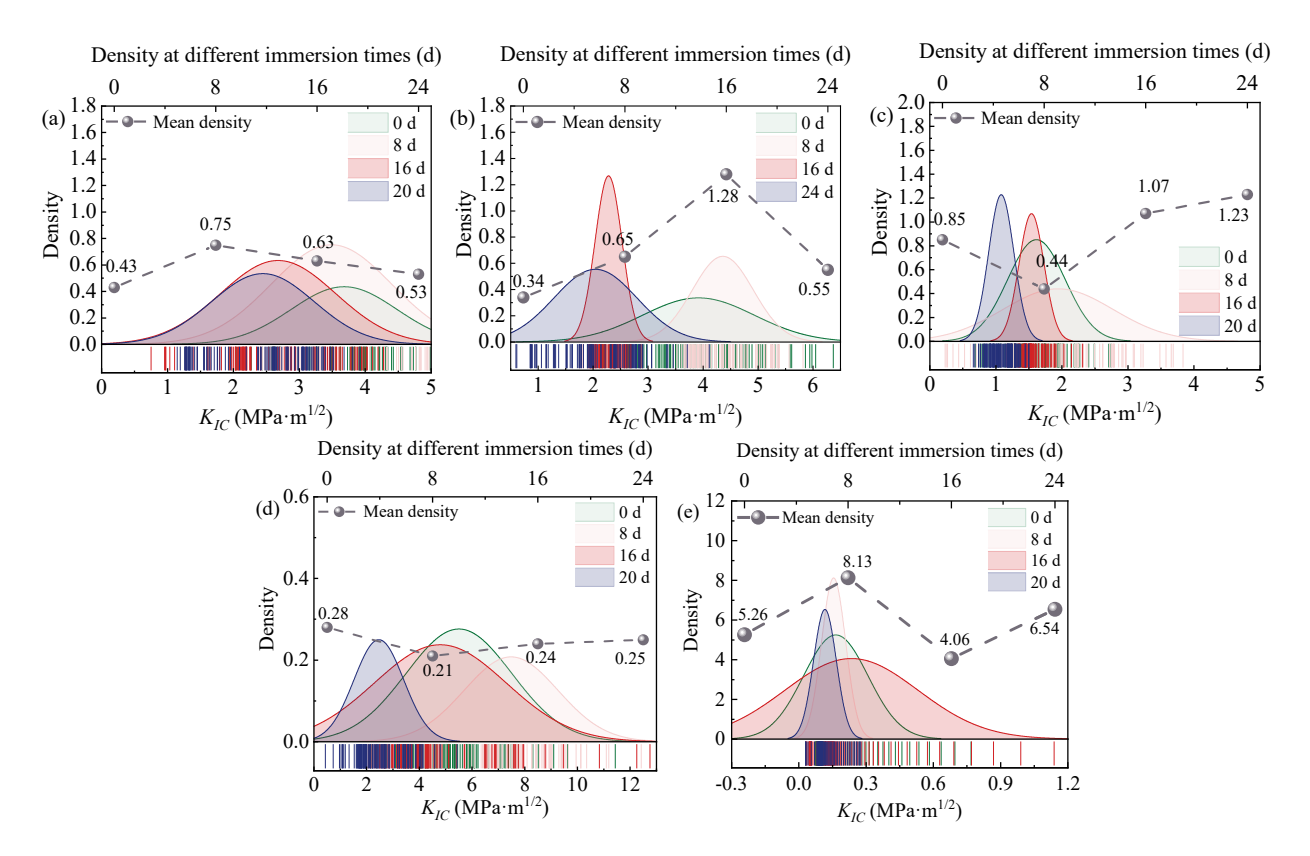


Fig. 12. Evolution of fracture toughness distribution: (a) Feldspar debris conglomerate, (b) subfeldspathic debris conglomerate, (c) feldspar conglomerate, (d) quartz conglomerate and (e) debris conglomerate.

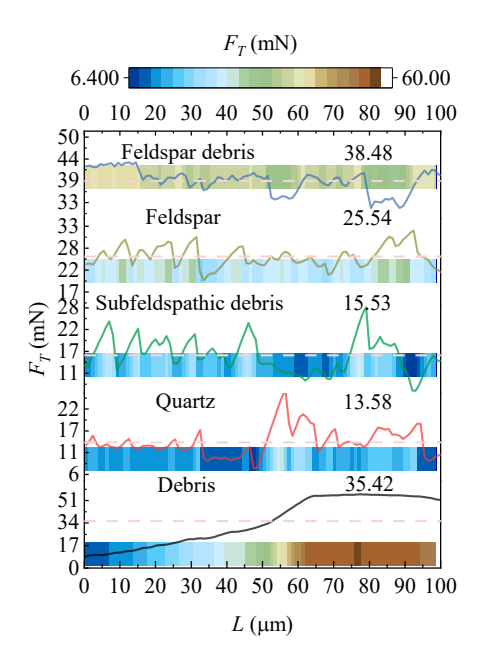


Fig. 13. Displacement-cutting force curve before scCO₂-water soaking.

mineral analysis section.

3.3.3 Elastic-plasticity

The displacement-cutting force curves are illustrated in Fig. 13. The cutting force of feldspar debris conglomerate, feldspar conglomerate, subfeldspathic debris conglomerate, quartz con-

glomerate, and debris conglomerate are 38.45, 25.54, 15.53, 13.58, and 35.42 mN, respectively. The color mapping of cutting force directly illustrates the cutting force distribution. It can be seen that the feldspar debris conglomerate exhibits the highest average cutting force, while the quartz conglomerate shows the lowest value. The cutting force curves for feldspar debris conglomerate, feldspar conglomerate, subfeldspathic debris conglomerate, and quartz conglomerate follow a sawtooth pattern with increasing scratch displacement, whereas the cutting force curve for debris conglomerate remains smooth as the scratch displacement increases.

In terms of scratch cutting force fluctuations, the failure mode of lithic conglomerate is characterized as a single ductile failure, while those of feldspar debris conglomerate, feldspathic conglomerate, subfeldspathic debris conglomerate, and quartz conglomerate comprise both ductile and brittle failures. Brittle failure shows larger fluctuation profiles, while ductile failure exhibits smaller fluctuation profiles. In this study, the ductile failure (plastic flow) portion of the cutting force curve is used to quantify the effect of scCO₂-water treatment on rock toughness. Furthermore, to determine rock toughness, the coefficient of variation from statistical analysis is introduced. A larger coefficient of variation indicates lower toughness, while a smaller coefficient of variation indicates higher toughness. The formula for calculating the coefficient of variation is as follows:

$$C_{v} = \frac{\sigma}{\bar{r}} \tag{8}$$

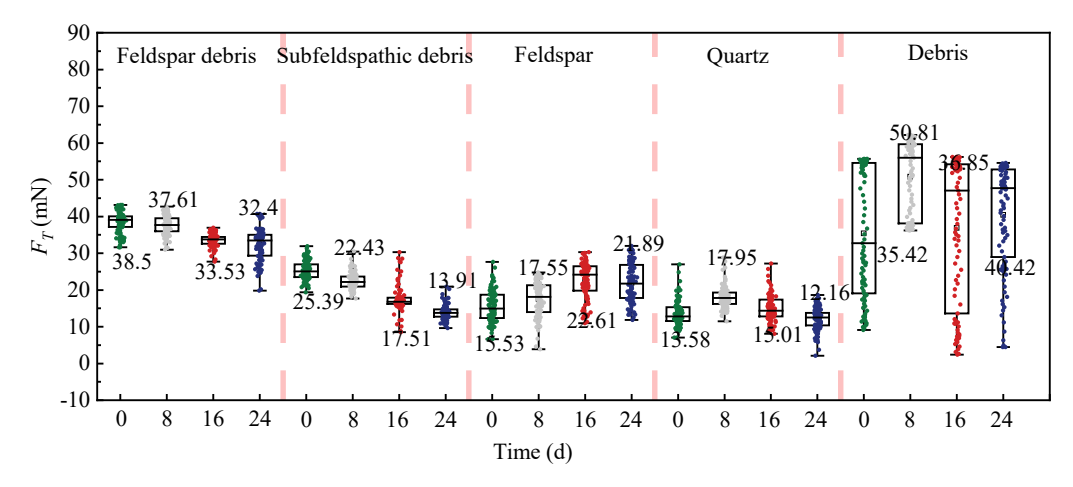


Fig. 14. Changes in cutting force after scCO₂-water immersion.

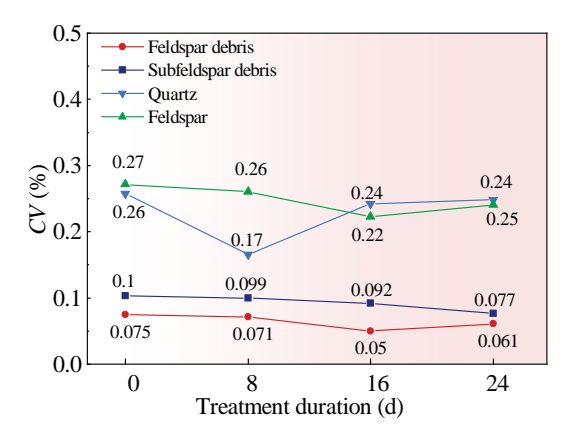


Fig. 15. Results of ductile failure change vs. immersion time.

$$\sigma = \sqrt{\frac{\sum_{i=1}^{n} (x_i - \overline{x})^2}{n}}$$
 (9)

where C_{ν} represents the coefficient of variation (dimensionless), σ represents the standard deviation, \bar{x} is the sample mean, x_i denotes the *i*-th value in the sample, and *n* represents the sample size.

The variations in cutting forces are illustrated in Fig. 14. After 24 d of immersion, the average cutting force of feldspar debris conglomerate, subfeldspathic debris conglomerate, feldspar conglomerate, quartz conglomerate, and debris conglomerate is 32.39, 13.91, 21.89, 12.16 and 40.01 mN, respectively. Among them, the cutting forces of feldspar debris conglomerate, subfeldspathic debris conglomerate, and quartz conglomerate decrease to some extent. In contrast, the cutting forces of feldspar conglomerate and debris conglomerate increase by 40.95% and 11.47%, respectively. With increasing soaking time, the cutting forces of feldspar debris conglomerate and subfeldspar debris conglomerate show a linear decreasing trend, while the scratch cutting forces of feldspar conglomerate, quartz conglomerate, and debris conglomerate initially increase and then decrease.

The statistical results of ductile failure under different soaking durations are shown in Fig. 15. Before soaking treatment, the coefficient of variation for feldspar debris conglomerate, subfeldspathic debris conglomerate, feldspar conglomerate, and quartz conglomerate is 0.075, 0.1, 0.27, and 0.26, respectively, which shows various degrees of reduction after scCO₂-water soaking for all four samples. Specifically, the coefficient of variation for feldspar debris conglomerate, subfeldspathic debris conglomerate, feldspar conglomerate, and quartz conglomerate decrease by 18.67% (0.061), 23% (0.077), 3.84% (0.25), and 11.11% (0.24), respectively. A smaller coefficient of variation indicates less fluctuation in the curve and stronger plastic flow, suggesting that scCO₂-water soaking enhances the toughness of feldspar debris conglomerate, subfeldspathic debris conglomerate, feldspar conglomerate, and quartz conglomerate. Among them, the reduction is greatest for subfeldspathic debris conglomerate and smallest for quartz conglomerate.

In conjunction with the cutting force changes (Fig. 15), scCO₂-water exerts the most significant impact on the toughness and cutting force of subfeldspathic debris conglomerate, and the least effect is on quartz conglomerate. Since the clastic conglomerate shows only a single failure mode (ductile failure), it can be inferred that the lithic content change in the conglomerate will affect the reaction degree of different rock samples. The greater the lithic content in the conglomerate is, the more pronounced the impact of scCO₂-water on its toughness and cutting force. Conversely, conglomerates with lower lithic content experience a smaller effect on toughness and cutting force.

4. Discussion

4.1 Mineral dissolution and precipitation

The physical and chemical properties of conglomerate are significantly influenced by the reactivity of minerals therein. As shown in Fig. 16, quartz (SiO₂) is a mineral found in almost all types of conglomerate and other rocks (Nesbitt and Young, 1984). The micro-scratch results indicate that quartz conglomerate exhibits the lowest values of maximum scratch depth and fracture toughness, indicating its high mechanical strength. However, after soaking in scCO₂-water for 24 d, the reduction in its fracture toughness is particularly significant.

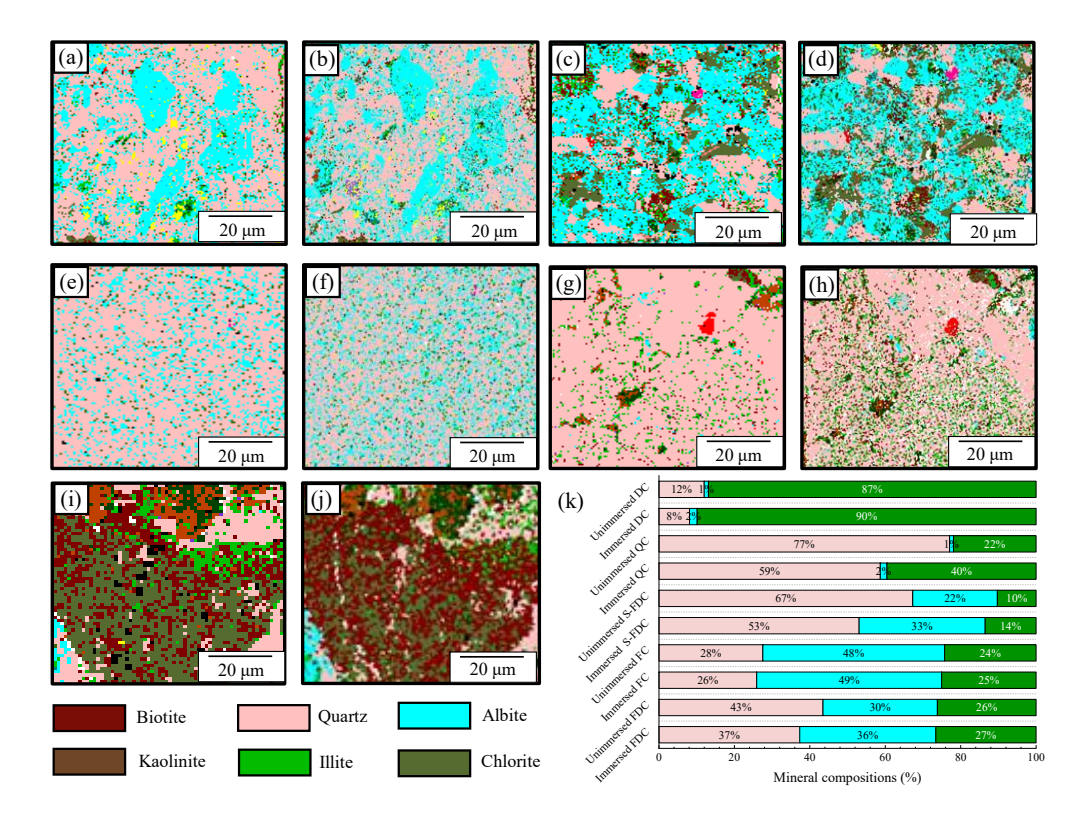


Fig. 16. Mineral composition changes: (a)-(b) Elemental variation in feldspar debris conglomerate, (c)-(d) elemental variation in subfeldspathic debris conglomerate, (e)-(f) elemental variation in feldspar conglomerate, (g)-(h) elemental variation in quartz conglomerate and (i)-(k) elemental variation in debris conglomerate.

This decrease in mechanical strength may be related to the dissolution process of quartz. Crundwell (2017) demonstrated that quartz can dissolve in water and proposed a related equilibrium equation, as shown in Eq. (10):

$$SiO_2 + 2H_2O = H_4SiO_4$$
 (10)

$$3 \text{ NaAlSi}_{3}O_{8} \text{ (albite)} + K^{+} + 2H^{+} + H_{2}O =$$
(11)

$$KAl_3Si_3O_{10}(OH)_2$$
 (illite) $+3Na^+ + 6SiO_2 + H_2O$

$$CO_2 + H_2O \leftrightarrow H_2CO_3 \leftrightarrow H^+ + HCO_3^-$$
$$\leftrightarrow 2H^+ + CO_3^{2-}$$
(12)

Illite +
$$1.1\,\text{H}^+ \leftrightarrow 0.77 \text{Kaolinite} + 0.6\,\text{K}^+ + 0.25\,\text{Mg}^{2+} + 1.2 \text{Quartz} + 1.35\,\text{H}_2\text{O}$$
 (13)

Consequently, quartz may undergo mechanical alterations after scCO₂-water treatment due to the dissolution and precipitation of SiO₂. On the other hand, the surface of quartz conglomerates exhibits an increase in clay mineral particles. Illite is a potassium-rich silicate clay mineral with relatively low mechanical strength. The rise in illite content could be a profound reason for the significant reduction in the strength of quartz conglomerates, feldspar conglomerates, feldspar debris conglomerates, and subfeldspathic debris conglomerates. The formation of illite occurs not only through the illitization of kaolinite and smectite but also due to the illitization of feldspar. According to Eq. (11), owing the chemical "compatibility" between albite and illite, albite can directly transform into illite under certain conditions (Xiong et al., 2022). After

CO₂ injection into the reservoir, it reacts with water to form carbonic acid solution, which dissociates to produce H⁺. The ions in the carbonic acid solution subsequently react with the silicate ions (SiO₄⁴⁻) dissolved from quartz, forming more soluble silicate ions. Consequently, a portion of the quartz dissolves, leading to a decrease in quartz content. Meanwhile, the sodium ions (Na⁺) in the carbonic acid solution can react with aluminum ions (Al3+) in the rock fragments, resulting in an increase in albite minerals. Therefore, the reduction of quartz content and the increase of illite content results from the reactions between ions in the carbonic acid solution and rock components. Furthermore, the transport effects of scCO₂-water cannot be ignored. It can be hypothesized that the formation of illite in the quartz region might be attributed to the transportation of illite minerals from other areas, leading to deposition and accumulation. However, testing this hypothesis requires further geological surveys and experimental analysis for validation.

The reactivity of minerals significantly impacts the conglomerate properties. For debris conglomerate, nonlinear deformation fluctuations (e.g., initial increase, transient decrease at 16 d, and rebound at 24 d in Fig. 10) arise not only from clay reorganization and secondary mineral formation but also from time-dependent swelling/shrinkage effects induced by scCO₂. Specifically, the hydration-driven swelling of clay minerals (e.g., kaolinite and illite) under acidic scCO₂ conditions causes initial volumetric expansion, increasing deformation. Subsequently, shrinkage occurs due to dissolution-induced

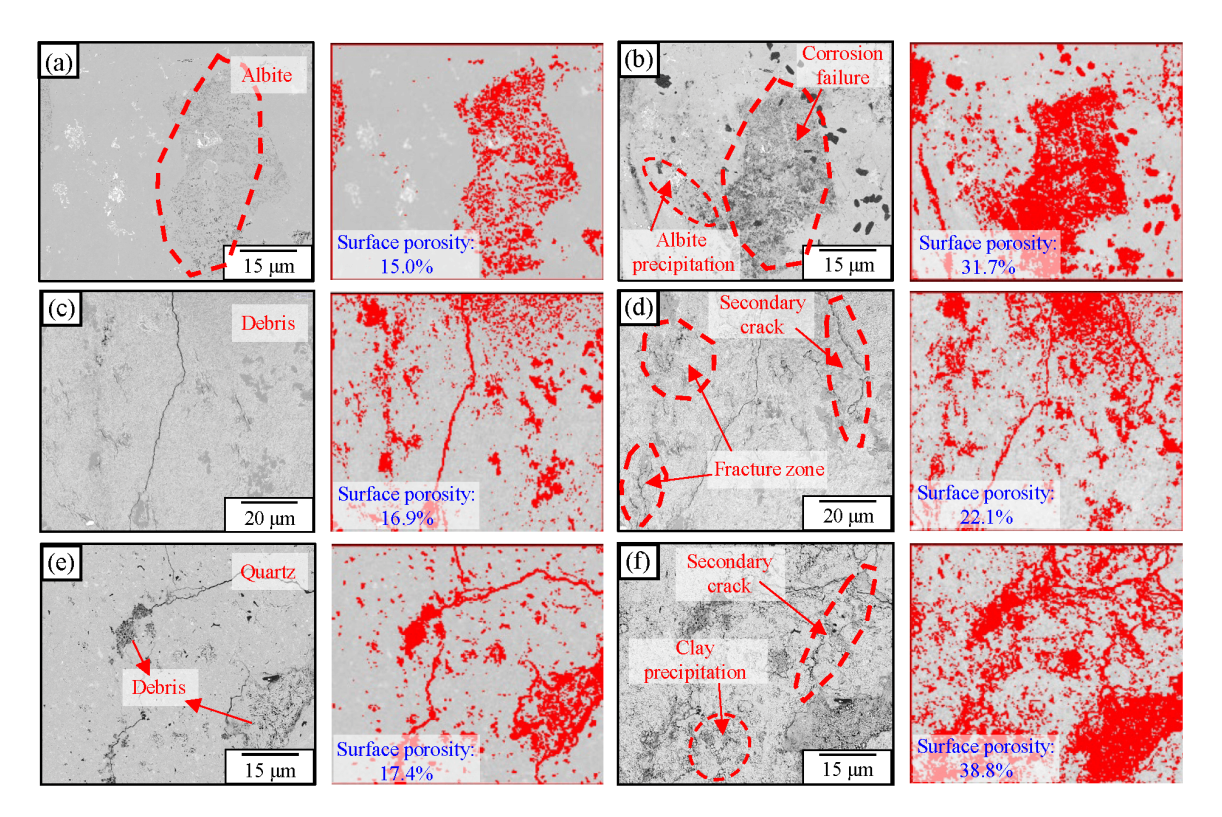


Fig. 17. SEM results after scCO₂-water immersion for 24 d: (a)-(b) Feldspar conglomerate, (c)-(d) debris conglomerate and (e)-(f) quartz conglomerate.

dehydration or mineral reprecipitation, explaining the transient decrease, which is corroborated by SEM observations in Figs. 17(c) and 17(d), showing localized volumetric strain from kaolinite swelling (highlighted by pore-filling textures) and shrinkage cracks from illite dehydration. Quartz dissolution (Eq. (10)) and albite-illite transformation (Eq. (11)) make a further contribution (Xiong et al., 2022), but swelling/shrinkage dominates in clay-rich debris conglomerate. The combined effects of processes such as swelling, shrinkage and secondary crack propagation underpin the non-monotonic mechanical response. To refine the predictive models, future studies should quantify the swelling coefficients under scCO₂.

The scratch results of clay indicate that both the fracture toughness and the scratch depth decrease after soaking, albeit to a minor extent. It is generally believed that clay minerals exhibit higher reactivity in terms of both chemical and mechanical properties. The changes in clay composition before and after soaking are illustrated in Figs. 16(i) and 16(j), respectively. It can be observed that illite reacts with carbonates to form kaolinite, as represented by Eq. (13) (Xiong et al., 2022; Zhou et al., 2025). Notably, similar clays exhibit minimal differences in mechanical strength, and their dissolution and precipitation processes are dynamically reversible. The reduction in mechanical strength of the conglomerate is primarily due to the expansion and transformation of clay minerals.

Feldspar exhibits relative inertness in its mechanical properties; however, it is chemically less stable, showing significant reactivity and a strong affinity for dissolution. The microscratch results reveal that the fracture toughness of feldspar debris conglomerate, feldspar conglomerate, and subfeldspathic debris conglomerate exhibit 33.42%, 48.72%, and 32.5% reductions, respectively, which are relatively similar figures. The mineral distribution before and after soaking for the three samples is shown in Figs. 16(a)-16(f), respectively. It can be observed that the content of feldspar mineral show 6%, 1%, and 5% increases, respectively, which figures somewhat deviate. This increase in feldspar content leads to the overall reduction in the strength of conglomerates. The observed increase in feldspar content might result from the scCO2water interaction on the distribution and concentration of residual feldspar around the gravel. As the carbonate solution partially dissolves the surface layer of feldspar, the remaining undissolved feldspar could be redistributed, leading to an apparent increase in feldspar content around the gravel.

While the dissolution of quartz, feldspar, and clay minerals (e.g., illite, kaolinite) dominates the observed mechanical degradation, the potential role of additional secondary minerals cannot be entirely dismissed. For instance, Fe-/Mg-bearing minerals (e.g., chlorite) may undergo oxidation or hydration under acidic scCO₂-water conditions, forming secondary oxides or hydroxides that weaken the grain boundaries. Although QEMSCAN and SEM observations focused on the major mineral phases, the identification of additional secondary minerals may require advanced techniques (e.g., TEM or XRD) for definitive confirmation. Future studies should prioritize these techniques to fully unravel the chemo-mechanical interplay in scCO₂-water-rock interaction (SCWRI) systems.

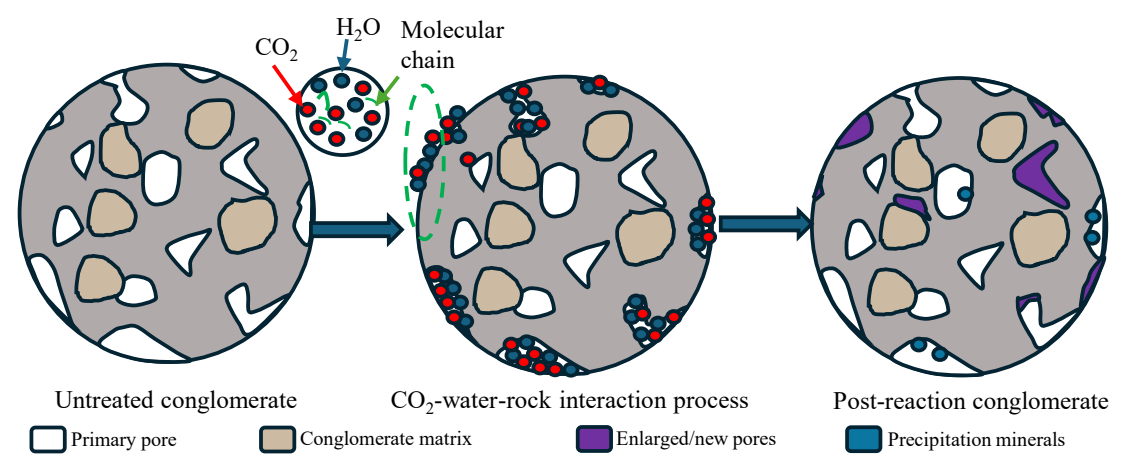


Fig. 18. Schematic diagram of CO₂ dissolution and sequestration.

4.2 Pore structure evolution

Mechanical degradation under the supercritical CO₂-waterrock interaction is initiated by the dissolution of CO₂ in water, forming a carbonic acid solution that infiltrates rock pores and fractures (Fig. 17). This reactive fluid penetrates micropores and mineral interfaces, triggering the dissolution of primary minerals (Wu et al., 2022). These reactions alter mineral composition and compromise structural integrity, as evidenced by post-immersion SEM images, which show roughened surfaces, enlarged pores and interconnected crack networks. Beyond primary mineral dissolution, SCWRI facilitates secondary mineral formation (Fig. 17). Illite accumulates at the quartzfeldspar boundaries, weakening intergranular cohesion and exacerbating fracture toughness reduction (e.g., 55.27% decline in quartz conglomerate). Concurrently, kaolinite precipitation induces localized volumetric strain through hydration-driven swelling (Fig. 17(d)), generating stress-concentrating microcracks that propagate along weakened clay interfaces (Figs. 17(b), 17(d) and 17(f)). These chemo-mechanical processes collectively degrade the macroscopic mechanical properties, transitioning failure modes from brittle fracture to ductile deformation.

4.3 Fluid occurrence

The evolution of pore structure arises from synergistic mechanisms involving physicochemical interactions. As illustrated in Fig. 18, scCO₂ dissolves in water to form a carbonic acid solution that adsorbs onto rock surfaces. scCO2 readily infiltrates into micropores, progressively enlarging them to become interconnected macropores. Concurrently, ion exchange within the solution facilitates the precipitation of secondary minerals, which partially occlude pore throats and disrupt connectivity. These processes align with prior studies on CO₂water-rock interactions. Mineral dissolution, secondary phase formation, and clay migration collectively degrade reservoir integrity (Zhang et al., 2020). Notably, density contrasts between dissolved primary minerals (e.g., albite) and precipitated secondary phases (e.g., illite) generate residual stresses, promoting interfacial debonding and secondary crack propagation (Figs. 17(e) and 17(f)). Feldspar dissolution further releases Na⁺ and Al³⁺ ions, which react with silicates to reprecipitate albite (Fig. 16(f)). These microstructural alterations correlate with NMR-derived pore homogenization (DN1: 5.43% reduction) and enhanced connectivity (Fig. 19). Collectively, these findings underscore the dual role of scCO₂ in reshaping both pore structure and mechanical behavior via chemo-mechanical coupling.

NMR was employed to characterize pore size distribution via T_2 spectrum analysis (Fig. 19(a)). The term "cumulative peak area" refers to the total integrated signal intensity under the T_2 relaxation curve, which is directly proportional to the total measurable porosity of the conglomerate (Wei et al., 2020). This parameter quantifies the total volume of fluidsaturated pores, encompassing both micropores and macropores. After 16 d of scCO₂-water immersion, the cumulative peak area increased by 18.22%, indicating a net increase in total porosity due to mineral dissolution and pore enlargement. Concurrently, the primary peak intensity (0.01-10 ms range) substantially increased, signifying growth in small pores (micropores/mesopores), while the secondary peak shifted toward longer T_2 times (10-100 ms), reflecting the enlargement of large pores (macropores). These changes align with SEMobserved microcrack proliferation (Figs. 17(b), 17(d) and 17(f)). Concurrently, the primary peak intensity substantially increased and the secondary peak shifted towards longer T_2 times. These changes indicate the increased abundance of small pores and enlargement of large pore sizes. The observed pore enlargement aligns with the increased microcrack density detected via SEM (as discussed previously). After 24 d of immersion, the cumulative peak area increase was significantly smaller (only 5.5%), suggesting sustained but diminished microstructural alteration. Comparatively, the damage to the pore structure was more pronounced during the early-stage immersion period.

Taking the distribution characteristics observed in T_1 - T_2 maps as a basis, distinct fluid components exhibit differentiated spatial distributions. This zonation follows the pore segmentation model along the T_2 dimension proposed by Sun et al. (2024). Distinct fluid components occupy specific regions within the T_1 - T_2 map. As depicted in Figs. 19(b) and 19(c),

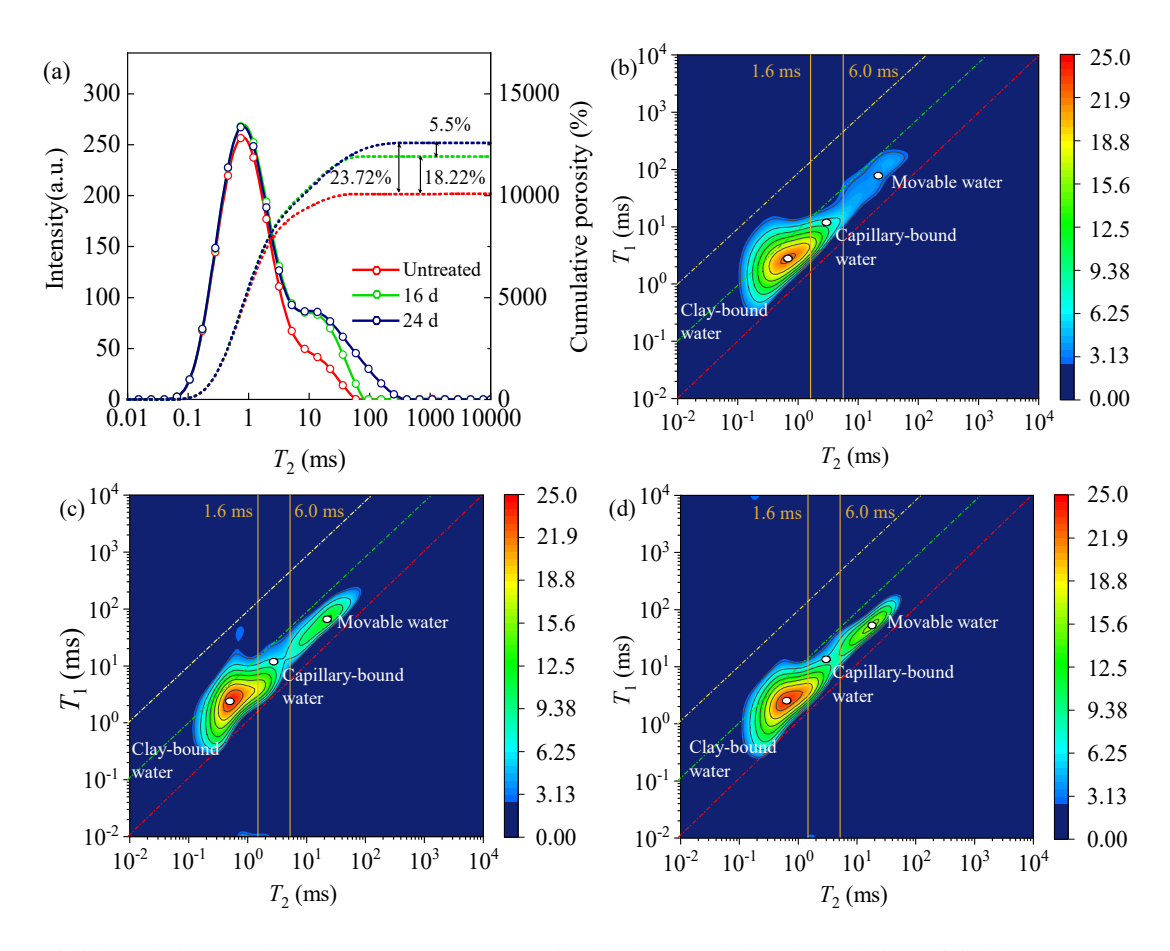


Fig. 19. Pore fluid evolution mechanisms: (a) T_2 spectrum distributions and (b)-(d) evolution of fluid occurrence states.

fluid signals are concentrated within three intervals: Claybound water ($T_2 < 1.6$ ms), capillary-bound water (1.6 ms $< T_2 < 6$ ms), and movable water (6 ms $< T_2 < 20$ ms). After 16 d of scCO₂-water immersion, the expanded signal areas and increased signal intensity (darker regions) indicate altered pore structure and increased water content within pores. Notably, the increased signal intensity for capillary-bound water suggests the enlargement of some micropores into small pores. A significant increase in movable water is also observed, corresponding to the T_2 spectral results. Following 24 d of immersion, the signal intensity increased across micropores/small pores and medium/large pores, indicating continued mineral reaction with CO₂.

5. Conclusions

In contrast to conventional macroscopic mechanical tests that often overlook localized mineral-scale responses, this study employed micro-scratch testing coupled with SEM and NMR to elucidate mineral-specific mechanical degradation and pore-scale structural evolution induced by scCO₂-water-rock interactions. Our findings revealed the following:

 While conventional macro-mechanical tests often fail to consider localized interfacial degradation, our microscratch analysis uncovered distinct failure modes among different conglomerate lithologies, governed by mineral hardness contrast and pore structure heterogeneity.

- 2) Contrary to the conventional view of uniform weakening, we observed non-monotonic changes in fracture toughness and deformation resistance (initial increase followed by significant decline), particularly in clay-rich conglomerates, due to the competing effects of mineral dissolution, illitization, and clay swelling/shrinkage.
- 3) The elective dissolution and migration of minerals induce secondary fractures, substantially weakening the mechanical integrity of the rock matrix. These promote pore connectivity through dissolution-transport processes, while the reduced surface roughness and pore complexity can accelerate the degradation of deformation resistance. These processes, visualized through *in-situ* scanning electron microscopy and nuclear magnetic resonance, have been rarely quantified in conventional macroscopic studies.

This study has certain limitations. While it primarily investigated the short-term effects (up to 24 d) of scCO₂-water-rock interactions on conglomerate mechanics and microstructure under specific thermodynamic conditions (70 °C, 10.34 MPa). The findings are based on samples from a single geological setting (Mahu area), while the long-term chemo-mechanical evolution (e.g., over years) remains unvalidated. Furthermore, the micro-scratch approach, while effective for surface micro-mechanics, does not fully capture the complex *in-situ* stress constraints and multi-physical field coupling (thermal-hydro-

mechanical-chemical, THMC) prevalent in actual reservoirs. Thus, future research should focus on: (1) Extending treatment durations and incorporating more diverse geological samples to enhance generalizability; (2) employing *in-situ* synchrotron or micro-CT techniques to visualize the dynamic processes of mineral dissolution and fracture propagation in real time under THMC coupling conditions; (3) developing multi-scale constitutive models that integrate the nano-mechanical properties obtained from scratch tests with macro-mechanical responses, ultimately improving the predictive capability for long-term reservoir integrity.

Acknowledgements

This work was supported by the National Natural Science Foundation of China (No. 52374014) and the Fundamental Research Funds for the Central Universities (No. 2024ZKPYSB03).

Conflict of interest

The authors declare no competing interest.

Open Access This article is distributed under the terms and conditions of the Creative Commons Attribution (CC BY-NC-ND) license, which permits unrestricted use, distribution, and reproduction in any medium, provided the original work is properly cited.

References

- Akono, A. T, Kabir, P. Microscopic fracture characterization of gas shale via scratch testing. Mechanics Research Communications, 2016, 78: 86-92.
- Akono, A. T., Randall, N. X., Ulm, F. J. Experimental determination of the fracture toughness via microscratch tests: Application to polymers, ceramics, and metals. Journal of Materials Research, 2012, 27(2): 485-493.
- Akono, A. T., Reis, P. M., Ulm, F. J. Scratching as a fracture process: From butter to steel. Physical Review Letters, 2011, 106(20): 204302.
- Akono, A. T, Ulm, F. J. Microscopic toughness of viscous solids via scratching: From amorphous polymers to gas shale. Journal of Nanomechanics and Micromechanics, 2017, 7(3): 04017009.
- Bai, B., Ni, H., Shi, X., et al. The experimental investigation of effect of supercritical CO₂ immersion on mechanical properties and pore structure of shale. Energy, 2021, 228: 120663.
- Bello, A. M., Al-Yaseri, A., Amao, A. O., et al. CO₂-Rock-Brine interactions in feldspar-rich sandstones that underwent intense heating. ACS Omega, 2024, 9: 31578-31585.
- Bull, S. J. Failure modes in scratch adhesion testing. Surface and Coatings Technology, 1991, 50: 25-32.
- Busch, A., Alles, S., Gensterblum, Y., et al. Carbon dioxide storage potential of shales. International Journal of Greenhouse Gas Control, 2008, 2: 297-308.
- Crundwell, F. K. On the mechanism of the dissolution of quartz and silica in aqueous solutions. ACS Omega, 2017, 2: 1116-1127.
- Daphalapurkar, P. N., Wang, F., Fu, B., et al. Determination of

- mechanical properties of sand grains by nanoindentation. Experimental Mechanics, 2011, 51: 719-728.
- Dong, X., Shen, L., Liu, X., et al. NMR characterization of a tight sand's pore structures and fluid mobility: An experimental investigation for CO₂ EOR potential. Marine and Petroleum Geology, 2020, 118: 104460.
- Donnelly, E., Baker, S. P., Boskey, A. L., et al. Effects of surface roughness and maximum load on the mechanical properties of cancellous bone measured by nanoindentation. Biological and Bioinspired Materials and Devices, 2004, 823: 103-108.
- Eleni, S., Lyesse, L. Insights into the interaction of a shale with CO₂. Solid Earth, 2022, 13: 1823-1841.
- Esatyana, E., Alipour, M., Sakhaee-Pour, A. Characterizing anisotropic fracture toughness of shale using nanoindentation. SPE Reservoir Evaluation & Engineering, 2021, 24(3): 590-602.
- Espinoza, N. D., Kim, H. S., Santamarina, C. J. CO₂ geological storage-geotechnical implications. KSCE Journal of Civil Engineering, 2011, 15(4): 707-719.
- Fatah, A., Bennour, Z., Mahmud, H., et al. Surface wettability alteration of shales exposed to CO₂: Implication for long-term integrity of geological storage sites. International Journal of Greenhouse Gas Control, 2021, 110: 103426.
- Figueiredo, B., Tsang, C., Rutqvist, J., et al. Coupled hydromechanical processes and fault reactivation induced by CO₂ injection in a three-layer storage formation. International Journal of Greenhouse Gas Control, 2015, 39: 432-448.
- Goodman, A., Sanguinito, S., Tkach, M., et al. Investigating the role of water on CO₂-Utica shale interactions for carbon storage and shale gas extraction activities-Evidence for pore scale alterations. Fuel, 2019, 242: 744-755.
- Hangx, S., Arjan, V. D. L., Marcelis, F., et al. The effect of CO₂ on the mechanical properties of the captain sandstone: Geological storage of CO₂ at the Goldeneye field (UK). International Journal of Greenhouse Gas Control, 2013, 19: 609-619.
- Jung, H. B., Um, W. Y., Cantrell, K. J., Effect of oxygen coinjected with carbon dioxide on Gothic shale caprock-CO₂-brine interaction during geologic carbon sequestration. Chemical Geology, 2013, 354: 1-14.
- Li, C., Ostadhassan, M., Guo, S., et al. Application of peak force tapping mode of atomic force microscope to characterize nanomechanical properties of organic matter of the Bakken Shale. Fuel, 2018, 233: 894-910.
- Liu, K., Jin, Z., Zakharova, N., et al. Comparison of shale fracture toughness obtained from scratch test and nanoin-dentation test. International Journal of Rock Mechanics and Mining Sciences, 2023, 162: 105282.
- Luo, X., Ren, X., Wang, S. Supercritical CO₂-water-shale interactions and their effects on element mobilization and shale pore structure during stimulation. International Journal of Coal Geology, 2019, 202: 109-127.
- Nesbitt, H. W., Young, G. M. Prediction of some weathering trends of plutonic and volcanic rocks based on thermodynamic and kinetic considerations. Geochimica et Cosmochimica Acta, 1984, 48(7): 1523-1534.

- Nie, Y., Wu, B., Zhang, G., et al. Microscale damage induced by CO₂ storage on the microstructure of sandstone coupling hydro-mechanical-chemical processes. Energy & Fuels, 2022, 36: 15023-15036.
- Nie, Y., Zhang, G., Xing, Y., et al. Influence of wateroil saturation on the fracture process zone: A modified dugdale-barenblatt model. Energies, 2018, 11: 2882.
- Niu, Q., Wang, X., Chang, J., et al. Influencing mechanisms of multi-scale pore-fracture responses of coals on their macro/micromechanical behaviors under ScCO₂ injection. Advances in Geo-Energy Research, 2024, 14(1): 64-80.
- Randall, N. X., Vandamme, M., Ulm, F. J. Nanoindentation analysis as a two-dimensional tool for mapping the mechanical properties of complex surfaces. Journal of Materials Research, 2009, 24(3): 679-690.
- Richard, M., Hari, V., Robert, C., et al. CO₂ as a fracturing fluid: Potential for commercial-scale shale gas production and CO₂ sequestration. Energy Procedia, 2014, 63: 7780-7784.
- Richard, T., Dagrain, F., Poyol, E., et al. Rock strength determination from scratch tests. Engineering Geology, 2012, 147: 91-100.
- Sakulich, A. R., Li, V. C. Nanoscale characterization of engineered cementitious composites (ECC). Cement and Concrete Research, 2011, 41: 169-175.
- Seyyedi, M., Mahmud, H. K. B., Verrall, M., et al. Pore structure changes occur during CO₂ injection into carbonate reservoirs. Scientific Reports, 2020, 10: 3624.
- Shi, X., Jiang, S., Wang, Z., et al. Application of nanoin-dentation technology for characterizing the mechanical properties of shale before and after supercritical CO₂ fluid treatment. Journal of CO₂ Utilization, 2020, 37: 158-172.
- Sun, F., Sun, J., Wang, M., et al. Analysis and application of fluid components in high-clay matrix shale oil: A case study of gulong shale oil. Energies, 2024, 17: 3770.
- Tan, J., Xie, B., Lyu, Q., et al. Mechanical properties of shale after CO₂ and CO₂-based fluids imbibition: experimental and modeling study. Rock Mechanics and Rock Engineering, 2022, 55: 1197-1212.
- Tao, J., Meng, S., Li, D., et al. Experimental study on the impact of CO₂ treatment on different lithofacies in shale oil reservoirs. Applied Sciences, 2022, 12: 2217.
- Vandamme, M., Ulm, F., Fonollosa, P. Nanogranular packing of C-S-H at substochiometric conditions. Cement and Concrete Research, 2010, 40: 14-26.
- Wei, B., Zhang, X., Liu, J., et al. Supercritical CO₂-EOR in an asphaltenic tight sandstone formation and the changes of rock petrophysical properties induced by asphaltene precipitation. Journal of Petroleum Science and Engineering,

- 2020, 184: 106515.
- Wu, S., Ge, H., Li, T., et al. Characteristics of fractures stimulated by supercritical carbon dioxide fracturing in shale based on acoustic emission monitoring. International Journal of Rock Mechanics and Mining Sciences, 2022, 152: 105065.
- Yang, K., Zhou, J., Xian, X., et al. Effect of supercritical CO₂-water-shale interaction on mechanical properties of shale and its implication for carbon sequestration. Gas Science and Engineering, 2023, 111: 204930.
- Yang, L., Ge, H., Shi, X., et al. The effect of microstructure and rock mineralogy on water imbibition characteristics in tight reservoirs. Journal of Natural Gas Science and Engineering, 2016, 34: 1461-1471.
- Yang, L., Yang, D., Li, Y., et al. Nanoindentation study on microscopic mineral mechanics and bedding characteristics of continental shales. Energy, 2024a, 312: 133614.
- Yang, L., Yang, D., Zhang, M., et al. Application of nanoscratch technology to identify continental shale mineral composition and distribution length of bedding interfacial transition zone-a case study of cretaceous qingshankou formation in gulong depression, Songliao Basin, NE China. Journal of Petroleum Science and Engineering, 2024b, 234: 212674.
- Xiong, Z., Cao, Y., Liang, C., et al. Origin and significance of authigenic quartz and albite in lacustrine calcareous fine-grained sedimentary rocks. Marine and Petroleum Geology, 2022, 143: 105799.
- Zhang, K., Lai, J., Bai, G., et al. Comparison of fractal models using NMR and CT analysis in low permeability sandstones. Marine and Petroleum Geology, 2020, 112: 104069.
- Zhang, Y., Lashgari, R. H., Sepehrnoori, K., et al. Effect of capillary pressure and salinity on CO₂ solubility in brine aquifers. International Journal of Greenhouse Gas Control, 2017, 57: 26-33.
- Zhang, Y., Lebedev, M., Sarmadivaleh, M., et al. Swelling effect on coal micro structure and associated permeability reduction. Fuel, 2016, 182: 568-576.
- Zhang, Z., Cai, J., Chen, F., et al. Progress in enhancement of CO₂ absorption by nanofluids: A mini review of mechanisms and current status. Renewable Energy, 2018, 118: 527-535.
- Zhou, J., Tian, S., Zhou, L., et al. Effect of sub-/super-critical CO₂ and brine exposure on the mechanical and acoustic emission characteristics of shale. Journal of Natural Gas Science and Engineering, 2021, 90: 103921.
- Zhou, H., Yan, T., Trivedi, J., et al. Investigating rock properties and fracture propagation pattern during supercritical CO₂ pre-fracturing in conglomerate reservoir. Advances in Geo-Energy Research, 2025, 17(2): 95-106.